

Joseph P. Cusumano

Department of Engineering
Science & Mechanics,
Pennsylvania State University,
University Park, Pennsylvania 16802
e-mail: jpc@crash.esm.psu.edu

David Chelidze

Department of Mechanical Engineering &
Applied Mechanics,
University of Rhode Island,
Kingston, Rhode Island 02881
e-mail: chelidze@egr.uri.edu

Anindya Chatterjee

Department of Mechanical Engineering,
Indian Institute of Science,
Bangalore, 560012,
India
e-mail: anindya@mecheng.iisc.ernet.in.

A Dynamical Systems Approach to Damage Evolution Tracking, Part 2: Model-Based Validation and Physical Interpretation

In this paper, the hidden variable damage tracking method developed in Part 1 is analyzed using a physics-based mathematical model of the experimental system: a mechanical oscillator with a nonstationary two-well potential. Numerical experiments conducted using the model are in good agreement with the experimental study presented in Part 1, and explicitly show how the tracking metric is related to the slow hidden variable evolution responsible for drift in the fast system parameters. Using the idea of averaging, the slow flow equation governing the hidden variable evolution is obtained. It is shown that the solution to the slow flow equation corresponds to the hidden variable trajectory obtained with the experimental tracking method. Thus we establish in principle the relationship of our algorithm to any underlying physical process. Based on this result, we discuss the application of the tracking method to systems with evolving material damage using the results of some preliminary experiments. [DOI: 10.1115/1.1456907]

1 Introduction

In Part 1 of this paper, motivated by the need to track damage evolution in machinery, we have developed a nonlinear method for tracking slowly evolving hidden variables. From this perspective, damage is a hidden process causing nonstationarity in a fast, directly observable dynamical system. The method uses a phase space formulation of the damage tracking problem, and uses a *tracking metric* developed using the short-time reference model prediction error. The method was successfully applied to an electromechanical experimental system consisting of a vibrating beam with a nonlinear potential perturbed by a battery powered electromagnet. The connection between the tracking metric developed in Part 1 and the hidden drift state variable was demonstrated empirically. It was shown that, as expected from the theoretical derivation of the method, the tracking metric is in a one-to-one relationship with the local time average of the measured voltage signal.

In this, Part 2, of our paper, a physics based mathematical model of the experimental system is used to study analytically the direct connection between the tracking metric and the hidden drift process. Numerical experiments performed with the model are used to validate the experimental method. The idea of averaging is then used to show that the output of the tracking method is in fact following the solution to the slow flow equation for the drifting process. This provides a physical interpretation for the output of the tracking algorithm, and shows how, in principle, the experimental method can be related to the physics of the damage process. Based on this physical interpretation, we return to the experimental application of the tracking method, and discuss some preliminary results for a system with a crack growing to failure.

In the next section, we develop the mathematical model of the battery discharge experiment using a lumped parameter, Lagrangian formulation of the electromechanical system. In Section 3, the tracking method developed in Part 1 is applied to the mathematical model in numerical experiments. Using the output from numerical simulations of the mathematical model, we are able to

validate the tracking algorithm. In Section 4, we discuss the method of averaging as it relates to our problem. Finally, in Section 5, we finish with concluding remarks.

2 Model Derivation

In this section we develop a physics-based mathematical model of the experimental system in order to validate and physically interpret the experimental results of Part 1. We emphasize that our purpose here is *not* to carry out exact system identification on the experimental system: rather, we aim to derive a model that possesses the essential features of the experimental system necessary to test the tracking method, and to demonstrate certain key theoretical ideas. In any case, the main simplifying assumptions used in constructing the model, together with the motives behind them, are specified in what follows.

It is well known that the vibrating beam system that is the basis of our experiment can be modeled with reasonable accuracy by a single degree of freedom Duffing oscillator with a two well potential [1], especially in the constrained form employed here [2]. Such dimensionality claims result from application of delay embedding theory [3,4], as well as from direct comparison of attractors from proposed low dimensional models. The situation is no different here: in the experimental study of Part 1, for the reference data set, the estimated average pointwise dimension was found to be $d_p = 2.82$, and the minimum required embedding dimension was found independently to be $d_e = 5$. These results are consistent with a driven single degree of freedom oscillator, which has a phase space dimension of 3. Furthermore, as shown in Section 4.3 of Part 1, the correlation dimension estimates computed over intermediate time scales throughout the experiment were found to all be less than 3.

Even though these can not be said to be true "attractor" dimensions (due to the nonstationarity of the system), these results suggest that it is reasonable to look for a single, one degree of freedom model of the mechanical system, valid throughout the range of the experiment, in which the potential energy is slowly drifting. The experimental system can be viewed as consisting of a mechanical subsystem (shown schematically in Fig. 1) coupled with an electromagnetic subsystem (see Fig. 2). This coupling has the following effects: as the battery discharges, the decrease of stiffness in the potential well of the electromagnet lowers the natural

Contributed by the Technical Committee on Vibration and Sound for publication in the JOURNAL OF VIBRATION AND ACOUSTICS. Manuscript received July 2001; revised December 2001. Associate Editor: M. I. Friswell.

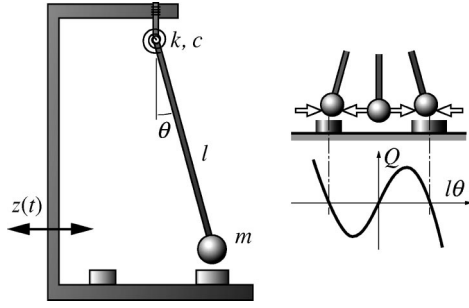


Fig. 1 Geometry of the mechanical subsystem: (left) single degree-of-freedom model of the constrained beam; (right) magnetic restoring force at beam tip

frequency of small oscillations in that well by a few percent (about 6 percent in the experiment); meanwhile, the beam motions parametrically excite the electromagnetic subsystem.

A lumped parameter model for the experimental system can be developed using Lagrange's equations. For simplicity, we neglect the effects of gravity; this introduces only a small nonlinear error term because the first-order effect of gravity can be incorporated into the torsion spring constant k in Fig. 1. In addition, we ignore energy losses due to eddy currents in the beam, assuming that all losses can be modeled using just a torsional damping coefficient c and circuit resistances.

Recently [5], it has been shown that the potential of the experimental system is not just a quartic two-well potential. However, in the interest of simplicity, and because it is entirely adequate for our purposes, here we employ a standard Duffing potential (P) of the form

$$P(\theta) = b_4\theta^4 + b_3\theta^3 + b_2\theta^2 + b_1\theta + b_0. \quad (1)$$

The model for the electromagnetic subsystem is shown schematically in Fig. 2, where: $\Phi(\epsilon t)$ ($\epsilon \ll 1$) is the slowly drifting battery open circuit voltage, taken to be its internal state; R_i is the internal resistance of the battery; R_e is the external resistance of the circuit; and L is the inductance of the electromagnet.

The inductance L is a function of the position of the beam. A simple model [6] that is adequate for our purposes is given by

$$L(\theta) = \frac{L_0}{1 + \kappa(\theta - \lambda)^2}, \quad (2)$$

where, L_0 , κ , and λ are positive constants.

Using a charge formulation [6] for the electromagnetic subsystem, the Lagrangian for the complete system can be expressed as

$$\mathcal{L} = \frac{1}{2}m(\dot{z} + l\dot{\theta})^2 + \frac{1}{2}L(\theta)\dot{q}^2 - \frac{1}{2}k\theta^2 - P(\theta), \quad (3)$$

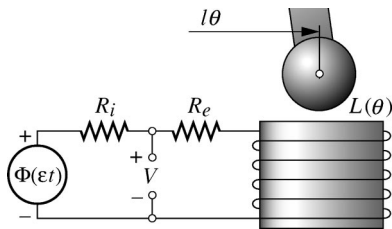


Fig. 2 Schematic diagram of the electromagnetic subsystem. The slowly decreasing open circuit battery voltage is $\Phi(\epsilon t)$, whereas the terminal voltage, which can be directly measured, is V .

where, m is the (effective) end mass, $z(t)$ is the imposed base excitation, and q is the net charge that has flowed out of the battery up to the instant of interest. The overdot denotes differentiation with respect to time.

The virtual work associated with nonconservative generalized forces (mechanical damping, electrical resistance and battery voltage) is

$$\delta\mathcal{W} = -c\dot{\theta}\delta\theta + (\Phi - R\dot{q})\delta q, \quad (4)$$

where $R = R_i + R_e$ is the total resistance of the circuit. Using Eqs. (3-4), Lagrange's equations yield:

$$ml^2\ddot{\theta} + c\dot{\theta} + k\theta + \frac{\partial P}{\partial \theta} - \frac{1}{2}\frac{\partial L}{\partial \theta}\dot{q}^2 = -ml\ddot{z}, \quad (5a)$$

$$L\ddot{q} + \left(\frac{\partial L}{\partial \theta}\dot{\theta} + R\right)\dot{q} = \Phi. \quad (5b)$$

We assume for simplicity that P is symmetric, i.e. $b_3 = b_1 = 0$ in Eq. (1). The force Q at the beam tip is then given by a cubic polynomial

$$\frac{\partial P}{\partial \theta} = -Q = a_3\theta^3 - a_1\theta, \quad (6)$$

where, $a_3 = 4b_4$ and $a_1 = -2b_2$ are positive constants. In Eq. (2) we use $\lambda = \sqrt{a_1/a_3}$ so that $L = L_0$ when the tip of the beam is directly above the electromagnet.

We set $-ml\ddot{z} = F \cos \omega t$ and define the new parameters

$$\omega_n^2 = \frac{k}{ml^2}, \quad \mu = \frac{c}{ml^2\omega_n}, \quad \alpha_i = \frac{a_i}{k} \quad (i=1,3),$$

$$f = \frac{F}{k}, \quad \Omega = \frac{\omega}{\omega_n}, \quad \text{and} \quad r = \frac{R}{L_0\omega_n}. \quad (7)$$

Then, rescaling time and defining dimensionless battery voltage and current variables by

$$\bar{t} = \omega_n t, \quad \phi = \sqrt{\frac{ml^2}{L_0}} \frac{\Phi}{k} \quad \text{and} \quad \psi = \sqrt{\frac{L_0}{ml^2}} \frac{dq}{d\bar{t}}, \quad (8)$$

Equation (5) can be written (after dropping the overbar from \bar{t}) in dimensionless form as:

$$\ddot{\theta} + \mu\dot{\theta} + (1 - \alpha_1)\theta + \alpha_3\theta^3 + \frac{\kappa(\theta - \lambda)}{(1 + \kappa(\theta - \lambda)^2)^2}\psi^2 = f \cos \Omega t, \quad (9a)$$

$$\frac{1}{1 + \kappa(\theta - \lambda)^2}\dot{\psi} + \left[\frac{2\kappa(\lambda - \theta)\dot{\theta}}{(1 + \kappa(\theta - \lambda)^2)^2} + r \right]\psi = \dot{\phi}, \quad (9b)$$

where the overdot now indicates differentiation with respect to the rescaled time as defined by Eqs. (7-8).

The time evolution of the battery voltage is governed by an electrochemical process that we do not explicitly model. Instead, given the experimental battery voltage evolution trends typically seen in the experiments (see Fig. 4 in Part 1 of this paper) we simply use the following voltage evolution law

$$\dot{\phi} = -\epsilon\psi(1 + \gamma(\phi - \eta)^2), \quad (10)$$

where γ and η are positive constants, and the rate constant ϵ satisfies $0 < \epsilon \ll 1$.

The battery model of Eq. (10) is a simple rate law capable of matching the qualitative characteristics of the battery discharge curves observed experimentally. It incorporates a linear dependence of the battery voltage drift rate on the current ψ in the circuit, which we expect to be reasonably accurate under the conditions seen in the experiments, since the external resistor R_e was chosen so that the current out of the battery was always positive. Previous experimental results, as well as the results of other re-

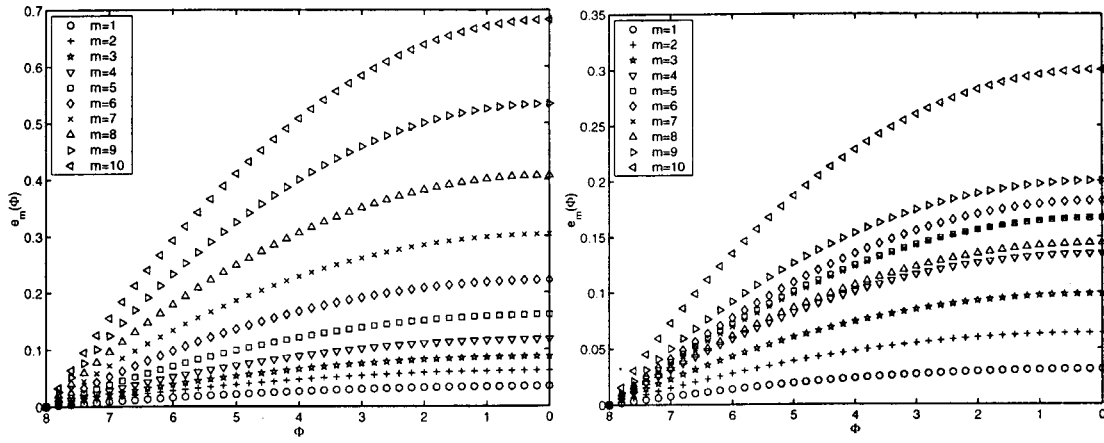


Fig. 3 Typical plots of numerically computed theoretical tracking functions, $e = \|e_k\|$, versus ϕ . Each figure is computed for a different randomly chosen initial condition. Curves are plotted for different prediction times, $t_p = mt_s$, with m ranging from 1 to 10.

searchers (see, for example, battery discharge curves in [7]), show that the battery voltage drops rapidly to the operating range and remains there for an extended period, slowly decreasing before another rapid drop to near zero voltage at the end of the battery's life. For constant ψ , the shape of $\phi(t)$ corresponds to the $\arctan[\sqrt{\gamma}(\phi - \eta)]$ function: this gives a similar trend to the one observed experimentally when η is equal to the mean value of the battery voltage in the operating range.

Equations (9-10) give a complete description of our system. Note that, in terms of the general hierarchical system description of Eqs. (1) in Part 1 of this paper, θ , $\dot{\theta}$ and ψ are the fast state variables (i.e., $\mathbf{x} = (\theta, \dot{\theta}, \psi) \in \mathbb{R}^3$), and the open circuit battery voltage ϕ is the hidden, slowly drifting variable ($\phi = \phi \in \mathbb{R}$).

For the analysis presented later, it is convenient to simplify our system further by making the following additional approximation. If we assume that the variable inductance coefficient κ in Eq. (2) is small ($\kappa \ll 1$), and that $r = \mathcal{O}(1)$ with respect to κ , then the current equation Eq. (9b) becomes

$$\dot{\psi} = \phi - r\psi + \mathcal{O}(\kappa). \quad (11)$$

The dimensionless parameter r can be interpreted as the ratio of the relaxation time scale for the electromagnetic subsystem (L_0/R) to the natural oscillation period of the mechanical subsystem, ($\propto 1/\omega_n$). In the experimental system, these two time scales were comparable, so it is reasonable to approximate ψ by its "quasi-steady state" value

$$\psi \approx \frac{\phi}{r}, \quad (12)$$

in the mechanical subsystem Eq. (9a) and battery evolution equation Eq. (10), since after only a few oscillations of the mechanical subsystem it will reach this value. This gives the *reduced* system

$$\ddot{\theta} + \mu\dot{\theta} + (1 - \alpha_1)\theta + \alpha_3\theta^3 + \frac{\kappa(\theta - \lambda)}{(1 + \kappa(\theta - \lambda)^2)^2} \left(\frac{\phi}{r}\right)^2 = f \cos \Omega t, \quad (13a)$$

$$\dot{\phi} = -\epsilon \frac{\phi}{r} (1 + \gamma(\phi - \eta)^2), \quad (13b)$$

with (referring once again to Eq. (1) in Part 1 of this paper) fast-time state variable $\mathbf{x} = (\theta, \dot{\theta}) \in \mathbb{R}^2$, and slow-time variable $\phi = \phi \in \mathbb{R}$.

Using Eqs. (9), the theoretical tracking function e_k , Eq. (14) in Part 1, can be computed numerically starting from any particular initial point $(\theta_0, \dot{\theta}_0, \psi_0)$ in the phase space of the fast subsystem. Starting from any randomly picked initial point in the phase

space, the state of the system at some later time $t_p = mt_s$, ($m = 1, 2, \dots, 10$) was calculated for different starting values of ϕ . The results of two such calculations are shown in Fig. 3 (for the simulation, we used parameters given in the following section). The typical plots in the figure show, as expected, that $e_k = \|e_k\|$ is a smooth function of ϕ . However, also as expected from the theoretical discussion of Part 1, while all curves have the same functional form, the *scaling* of each depends on $\mathbf{x}_0 = (\theta_0, \dot{\theta}_0)$: these changes in scaling correspond to changes in the coefficients of the mapping (Eq. (5) of Part 1) that relates the tracking function to the hidden variable.

Note that in this case all of the theoretical tracking curves are quadratic in ϕ (see Fig. 3). Thus, the tracking function is linearly related to the *square* of the battery voltage variable. This is a consequence of the physics included in our model: in Eqs. (13), ϕ enters into the fast subsystem via an inductive coupling term, and hence only as ϕ^2 . Therefore $\mu(\phi) = \mu(\phi^2) = \kappa\phi^2/r$, and hence the Taylor expansion Eq. (4) in Part 1, should be in terms of ϕ^2 , not just ϕ .

Since our primary interest is in testing the performance of the tracking algorithm, this particular deviation from the experiment does not present any difficulties. Indeed, the fact that the tracking method still works, as shown in the next section, demonstrates an important additional feature of the theory outlined in Part 1: even when linear observability fails, higher order observability is still possible (in this case, quadratic). When calibration data is available, the nature of the observability will typically be evident just from statistical analysis of the tracking output, as discussed below.

3 Simulation of the Model

We now describe numerical simulations of the complete system of Eqs. (9-10), which were carried out to investigate the performance of the tracking technique. The equations were integrated numerically with a standard 4th-order variable-step-size Runge-Kutta algorithm. The parameters for the model were not explicitly identified from experiments; however, they were selected to match the properties of the experimental system in key ways, as we now describe.

In choosing the parameters, we made sure that the change in the natural frequency of small oscillations in the potential well with the electromagnet was 6 percent (as was the case with the experimental system). The ratio of the forcing frequency and the system's first natural frequency was the same as for the experimental system. The effective mass $m = 0.4$ kg, and length $l = 0.128$ m,

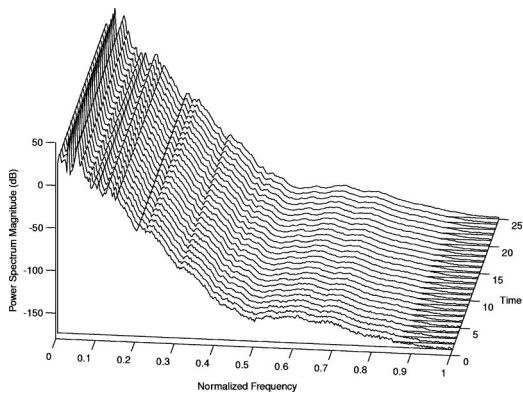


Fig. 4 Power spectra showing that the system is predominantly chaotic throughout the simulated experiment. 25 spectra are shown, each using 100,000 data points (Time is in units of $100,000/t_s$). Note the strong periodic window occurring during the 14th power spectrum calculation.

were obtained directly from the experiment. A fourth order polynomial fit to a histogram of the experimental reference data was used to estimate $\alpha_1 = 2.6558$ and $\alpha_3 = 0.8805$.

By linearizing Eqs. (9-10) about the stable equilibria ($\theta = \pm \sqrt{(\alpha_1 - 1)/\alpha_3}$) for $\Phi = 0$, expressions for the frequency of small oscillations were obtained, and used to estimate the effective stiffness k using Eqs. (7): since the frequency for $\Phi = 0$ in the electromagnet's well was 8.56 Hz, one can estimate $k = 0.145$ using m , l , and α_1 . Similarly, for $\Phi = 9$, the natural frequency in the electromagnet's well was 8.83 Hz. Using this information one finds $\kappa = 0.07$ after arbitrarily setting $r = 8$.

Other parameters used in the simulations were: $\Omega = 1.7608$, $f = 1$, $\eta = 10.539$, $\gamma = 1$ and $\epsilon = 5.5 \times 10^{-6}$. The forcing amplitude was selected to ensure that the system was nominally chaotic* throughout most (if not all) of the parameter range (see the power spectra in Fig. 4). Using the above parameters, one has $\phi = 1.7565 \Phi$, and the observed fast-time dynamics of the simulated

*No tests for chaos were performed for these numerical experiments, since the existence or nonexistence of chaos is not particularly relevant to the task at hand, as discussed in Part 1. In any case, given the nonstationarity of the Duffing subsystem, the system can at most be treated as only nominally chaotic, as indicated by broadband power spectra, positive finite time Lyapunov exponents, etc., over intermediate time scales.

θ were found to have qualitatively similar trajectories in the $(\theta, \dot{\theta})$ phase space to those observed with experimental strain-gauge time series.

The simulation used the complete system of Eqs. (9)–(10): 2.5×10^6 points were collected with a sampling time of $t_s = 0.2$. At the end of the simulation, ϕ reached a near-zero value. Average mutual information and false nearest neighbors algorithms were used to select a delay $\tau = 4$ sample steps, and an embedding dimension $d = 5$ (which, we remark, is the same as was obtained for the experimental data). After waiting an initial period to allow transients to die off, the first 2^{15} data points of the scalar θ data set were used for the reference model.

For the tracking metric e_4 (see Eq. (14) in Part 1), the entire reconstructed data set was divided into consecutive data records of size 2^{12} points each (i.e., $M = 2^{12}$), and 16 nearest neighbors were used for the reference model. The average pointwise dimension of the reference data set, used to compute e_4 , was $d_p = 2.87$. Figure 5 (left) plots the moving average of the tracking metric, \bar{e}_4 , versus the square of the moving average of the battery voltage, i.e., $\bar{\phi}^2$. In the figure, moving averages were done over $N_R = 10$ consecutive data records. The figure shows that the tracking metric computed by the algorithm is well described by an affine transformation of $\bar{\phi}^2$. Thus, we have demonstrated that the tracking algorithm recovers (to within an affine transformation) the theoretical tracking curves as shown in Fig. 3.

The accuracy of this fit (the solid gray line in Fig. 5, left) to the tracking output was further tested by calculating the mean polynomial fit errors for different fit orders. The top right sub-plot in Fig. 5 (left) shows that the error for the fit is not significantly reduced by using higher-order polynomials. Using the linear fit, the tracking metric was calibrated so that its range corresponded to the actual range spanned by ϕ . After scaling, the tracking metric and the corresponding value of $\bar{\phi}$ were plotted on the same graph (see Fig. 5, right). From this figure it is apparent that the observer provides a very good estimate of the change in the drifting variable.

Both Fig. 5 (left), in the bottom right corner, and Fig. 5 (right), in the top left corner, show that the tracking metric has some initial bias. As in the experiments, this is due to the fact that the local linear models are imperfect, and there is some initial error in prediction even for the reference data set. This initial error for the model data was on the order of 10^{-3} , whereas the same error for the actual experimental data was 10^{-2} . This order of magnitude difference in reference model accuracy accounts for the very small

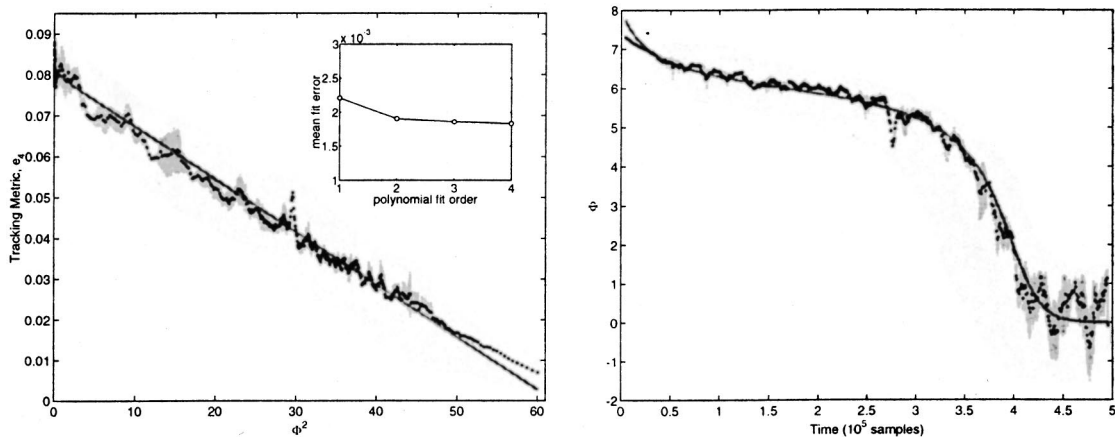


Fig. 5 Tracking results from numerical simulations: (left) Plot of \bar{e}_4 versus $\bar{\phi}^2$. Solid gray line shows a linear fit to the data. Top right corner sub-plot shows the mean fit error versus order of the fit. (right) Plot of the battery voltage $\bar{\phi}$ (solid gray line) vs. time, overlaid with the tracking metric \bar{e}_4 (black dots). For both plots, ten consecutive data records of size 2^{12} were used to calculate \bar{e}_4 and its statistical fluctuation (gray background shows \pm one standard deviation from the sample mean).

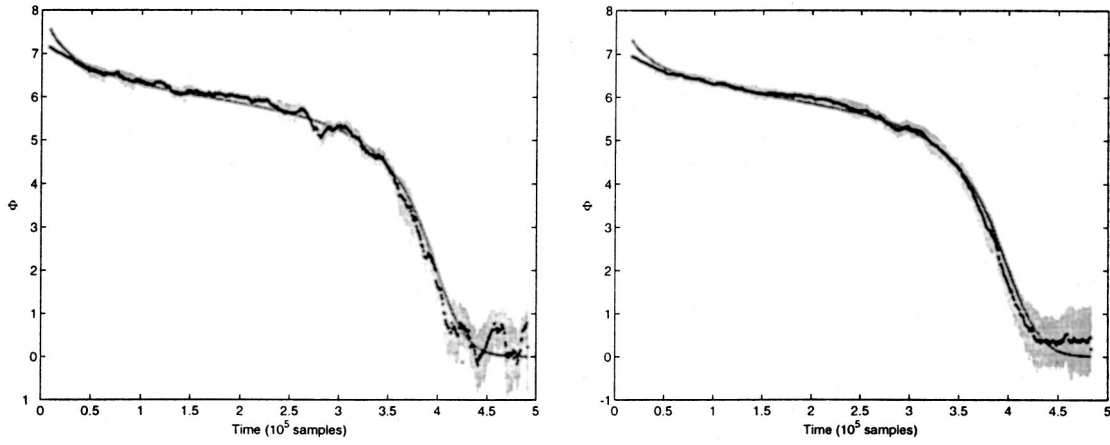


Fig. 6 Additional tracking results showing the effect of increasing the number of consecutive records N_R used for \bar{e}_4 : (left) $N_R=20$: (right) $N_R=40$. See Fig. 5 for plot details. As in the experimental results, the different values of N_R affect only the local fluctuations of the tracking, not the general trend. See text for additional discussion.

variance in the observer estimate for the simulations as compared to the experiments. On the other hand, the large variance at the end of the simulation is due to the square root scaling of the observer output with respect to ϕ , as discussed at the end of Section 2.

Recall from Part 1 that the moving average \bar{e}_k is carried out to compensate for fluctuations in the tracking metric caused by changes in the population of initial conditions used to compute the tracking function e_k . These fluctuations are caused by bifurcations that occur in the fast system as the slowly drifting variable evolves. In the numerical experiments, a rather strong example of such a fluctuation is visible near a time equal to about 2.7×10^5 samples, where a clear periodic window was encountered (refer once again to Figs. 4 and 5). This periodic window is responsible for the small local dip in \bar{e}_4 for $N_R=10$, a dip which can be largely eliminated by increasing N_R , as shown in Fig. 6. As in the laboratory experiments, the general trend of the tracking metric follows the local mean of the battery voltage quite well for all values of N_R . Increased values of N_R serve to stabilize somewhat the population of initial conditions used to compute e_4 , and thus smooth the tracker output.

4 Averaging of the Model Equations, and Comparison With Tracking

In this section, we demonstrate that the experimental tracking procedure developed in Part 1 is, in some sense, an experimental realization of the perturbation method of averaging. In particular, we show that the tracking metric follows the solutions to the *slow flow* equation governing the evolution of ϕ .

Recall the general form of the system with evolving damage, Eqs. (1) of Part 1:

$$\dot{\mathbf{x}} = \mathbf{f}(\mathbf{x}, \boldsymbol{\mu}(\phi), t), \quad (14a)$$

$$\dot{\phi} = \epsilon \mathbf{g}(\mathbf{x}, \phi, t). \quad (14b)$$

The relationship between what are typically considered to be damage evolution laws in the literature, and slow flow equations for coupled systems of the form of Eqs. (14) has been proposed in [8]: the discussion of averaging given below follows closely the treatment therein.

The method of averaging is a well known approximate analytical method [9], that can, under certain circumstances, be applied to systems of the above form. However, a key requirement for application of the analytical method is that an explicit solution to the unperturbed ($\epsilon=0$) system be available. In our context, we do not assume that such a solution is available: indeed, for our ex-

periments the $\epsilon=0$ reference system is *chaotic*, and thus an unperturbed analytical solution does not exist. Nevertheless, the concept of averaging can still be used, not as an analytical technique, but as a physical principle valid for systems in the form of Eqs. (14) with sufficient time scale separation (i.e., for which ϵ , and hence the damage growth rate, is sufficiently small). Thus, as employed here, our use of the idea of averaging cannot be said to be rigorous and analytical, but is rather heuristic and numerical.

Another key distinction between the discussion of averaging presented here and the classical perturbation method is that we are only really concerned about its effect on the hidden variable that we are trying to track, namely, ϕ . The averaged equations for the fast variable, \mathbf{x} , do not concern us.

To proceed, we consider the system of Eqs. (14), but with scalar quantities $\mathbf{g} \equiv g$, $\boldsymbol{\mu} \equiv \mu$, and $\boldsymbol{\phi} \equiv \phi$, as in the case studied here. Let $\mathbf{X}_0(\mathbf{x}_0, \mu(\phi_0), t)$ be the solution to the unperturbed Eq. (14a) with $\epsilon=0$, $\phi = \phi_0$, and initial conditions $\mathbf{x}(t_0) = \mathbf{x}_0$. We insert \mathbf{X}_0 into the right hand side of Eq. (14b), and define

$$\bar{g} := \lim_{T \rightarrow \infty} \frac{1}{T} \int_{t_0}^{t_0+T} g(\mathbf{X}_0(\mathbf{x}_0, \phi, t), \mu(\phi), t) dt, \quad (15)$$

where ϕ_0 in \mathbf{X}_0 has been replaced by the slowly drifting quantity ϕ , which is nevertheless treated as a constant in the integral. We assume that \mathbf{X}_0 , the solution to the unperturbed or nondrifting fast-time equation, has transients which decay rapidly, and converges to some well-defined steady-state behavior. Under this assumption, the integral above is independent of t_0 and \mathbf{x}_0 , and \bar{g} depends only on ϕ . We write,

$$\dot{\phi} = \epsilon \bar{g}(\phi). \quad (16)$$

The solutions to the averaged Eq. (16) approximate the evolution of ϕ wherever the assumptions about \mathbf{X}_0 are correct. Our goal is to compare the predictions of this slow flow equation obtained from the model of Eqs. (13) with the true evolution of ϕ obtained from numerical simulations. Note that the definition of the \bar{g} , in Eq. (15), can be implemented numerically even when analytical results are not available. Furthermore, the limit as $T \rightarrow \infty$ in practice is replaced by some fixed sufficiently large T corresponding to the intermediate time scale over which the fast time data is collected. More precisely, T corresponds to the time over which the N_R consecutive records used in each moving average \bar{e}_k are collected.

The fact is, however, that in this case (by design), we can do a little better, and an approximate analytical solution to the averaged system can be obtained. Since $\kappa=0.07$ and $r=8$ in the simulations, as previously discussed, the complete system of equations

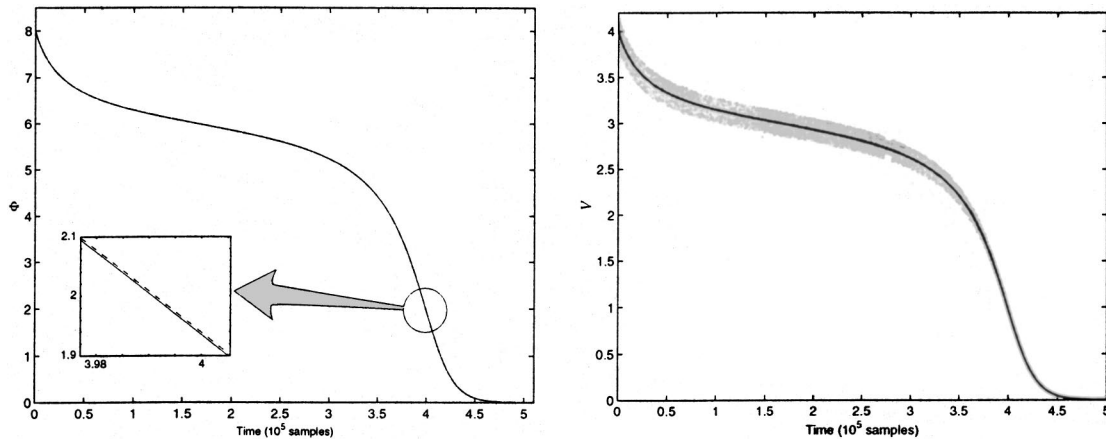


Fig. 7 Solutions to the slow flow equation: (*left*) Comparison of the slow flow solution Eq. (18), dashed line, to actual moving average $\bar{\phi}$, solid line, of the slow variable drift computed with the exact Eqs. (9), (10); (*right*) For comparison with the experiments, the *unaveraged* time series of the terminal voltage V (see Fig. 2) is plotted in light gray together with the slow flow solution. See text for additional details.

(9)–(10) is well approximated by the reduced system of Eqs. (13). Under the quasi-steady-state assumption on ψ used to derive Eqs. (13), we find that explicit calculation of the averaged vector field is not needed since Eq. (13b) is *already* in the form of the slow flow equation:

$$\bar{g} \equiv -\frac{\phi}{r}(1 + \gamma(\phi - \eta)^2), \quad (17)$$

which, from Eq. (16), gives:

$$\ln \left[\frac{\phi}{\sqrt{1 + \gamma(\phi - \eta)^2}} \right] + \eta\sqrt{\gamma} \arctan(\sqrt{\gamma}(\phi - \eta)) = (1 + \gamma\eta^2)(-\epsilon t/r + K). \quad (18)$$

In the above solution, the constant K is determined by the initial condition $\phi(0) = \phi_0$. For our set of parameters $K = 0.1337$. Figure 7 (left) shows the comparison between the solution of the slow flow equation with the value of ϕ obtained from numerical solutions to the exact system. The match is good to $\mathcal{O}(\kappa)$, as expected. For direct comparison with the experiments of Part 1, Fig. 7 (right) shows the solution to the slow flow equation plotted together with the unaveraged time series of the terminal voltage, V , corresponding to the experimentally measured electrical variable. V can be obtained from a simple circuit analysis of Fig. 2, which gives $V = \Phi - R_i \dot{q}$. After using the scalings of Eqs. (7) and (8), this can be rewritten as $V = \Phi - R_i \sqrt{k/L_0} \psi$. Thus, the simulation results for ψ and Φ can be used to plot V . The solution to the slow flow equation can then be plotted on the same scale using the relation Eq. (12).

By comparing Fig. 5 with Fig. 7, it is clear that the tracking metric follows the solution to the slow flow equation. That this should be true in general is not surprising, since the tracking metric is actually constructed from locally time averaged quantities (i.e., from moving averages across a few consecutive data records). In this case, it is possible to do this direct comparison between the tracking output and the slow flow solutions because the modeling strategy that was adopted made the analysis tractable. However, one should not expect to be able to perform a similar analysis for arbitrary systems: in many cases, the form of the evolution law for the hidden variable is unknown; and even if it is known, carrying out the averaging for arbitrary reference signals is in general not a trivial matter.

The important point here is that we have demonstrated *in principle* how the tracking metric computed from the short-time reference model prediction error can be related to the underlying

damage (or drift) physics. This means that when physics based damage models *are* available, they can be tested using the damage tracking algorithm presented here. Furthermore, we would argue on practical grounds that for true *prognostics*, tracking the slow flow damage dynamics is precisely what is needed to obtain useful predictions of remaining useful life of a machine or component: one is then not so much concerned with short term fluctuations, but with the general trend.

5 A System with Material Damage: Preliminary Results

After the general derivation of the tracking algorithm in Part 1, we have focused on a system in which “damage” is interpreted in terms of a hidden power source which fails over time. Using this electromechanical system, we have established the basic properties of the tracking metric and shown how it can in principle be related to the underlying physics of the damage process.

We now turn to briefly discuss the case of a system with evolving material damage. In particular, we examine a version of the two-well oscillator experiment in which a crack is allowed to grow to failure. To perform the experiment, the same two-well oscillator system described in Part 1 was used, except without the electromagnetic perturbation to its potential energy. Instead, a small notch was filed at the clamped end of the beam, and the system was started and then run to the point of complete fracture of the beam. In this case, a first principles model of the hidden variable is not so easy to obtain, and in the current experimental setup an independent measurement of the crack growth was not available.

Except as noted in what follows, the experimental parameters for this trial were identical to the experiment of Part 1. Again, only strain gauge data was collected. The first 2^{15} data points were used for the reference data set, and 16 nearest neighbors were used for the local linear model parameter estimation. The delay time τ and embedding dimension d in were both estimated to be 5. The pointwise fractal dimension for the reference data set was found to be $d_p = 2.7$. The tracking metric e_5 was estimated using 2^{12} point length consecutive data records.

Figure 8 shows the results of the tracking calculation for the system. Black dots in the figure indicate 10 data record average of e_5 , while the gray background depicts \pm one standard deviation. Complete failure of the beam occurred at 2.5 hours. Up until that point, the tracking output shows a relatively smooth, monotonic increase.

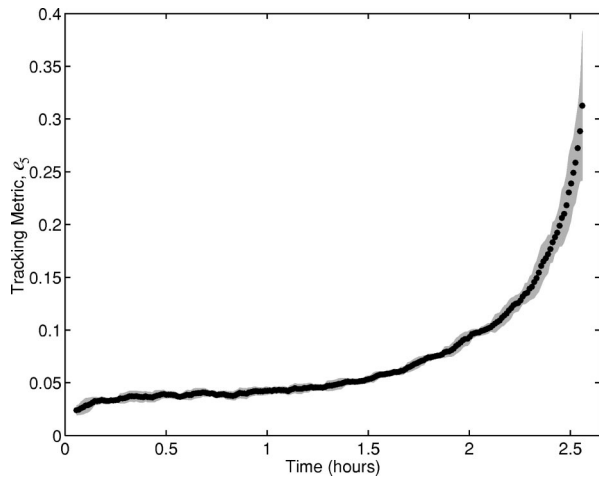


Fig. 8 Damage tracking results for the two well oscillator experiment with a crack growing to failure (see text for details). Black dots represent the tracking metric $\bar{\epsilon}_5$, computed from $N_R=10$ consecutive data records, plotted as a function of time. Light gray outline is drawn at \pm one standard deviation of the local mean.

It is worth pausing to consider the meaning of this result. The actual time history of the strain signal, as in the previous experiment, is complex, containing passages from nominally chaotic to nominally periodic responses and back again. Thus, the actual load history at the crack is anything but periodic. Yet, the result clearly shows a simple power-law like behavior. Based on the results in the previous sections, we interpret this as (to within some affine transformation) the solution to the slow flow dynamics of the actual damage rate law: it is precisely the local averaging in the tracking algorithm, combined with the finite time prediction error used to generate the tracking metric, that results in the relatively smooth tracking output, even for a complex load history. This suggests that the tracking algorithm discussed here can be used to generate data useful for the *construction* of damage evolution rate laws. This is the subject of our current research efforts.

6 Conclusions

In this two part paper, we have presented a new, phase-space-based algorithm capable of tracking the evolution of hidden damage or damage-like variables. The method uses only readily available “fast time” data from the directly-observable system. It uses average short-time reference model prediction error to obtain a tracking metric. This approach was successfully applied experimentally in Part 1. In Part 2, a physics-based model of the experiment was developed and used in numerical experiments to validate the algorithm.

We have also shown how the tracking output can, in principle, be related to the underlying physics of the problem. In general, the analytical treatment of drift in systems such as those studied here will involve averaging of the underlying system equations: though the system studied here permits a simpler analytical treatment, it still demonstrates the main idea that the tracking metric generated by the algorithm approximates the solutions to the hidden variable’s slow flow equation. The explicit connection made in this Part 2 of our paper between hidden variable drift and the drift observable gives us assurance that, in other situations where a first principles model is not available, the observable generated by the tracking algorithm can still be used with confidence and interpreted in a meaningful way.

To demonstrate the applicability to systems with material damage, some preliminary results for a system with a crack growing to failure were presented. It was found that the tracking metric provided a smooth observable that monotonically increased to the point of complete failure of the beam.

In the work presented here, we have applied our method in the simplest situation, namely that in which the forcing, load and environmental conditions are stationary. As with all other diagnostic/prognostic procedures, it is necessary to control (or account for) changes in the system caused by these factors in order to successfully interpret the tracker output in terms of the damage state. In future work we will address the issues of damage tracking in changing operational/environmental conditions.

Acknowledgments

This work was supported by the Office of Naval Research MURI on Integrated Predictive Diagnostics, Grant #N0014-95-0461.

References

- [1] Moon, F. C., and Holmes, P., 1979, “A Magnetoelastic Strange Attractor,” *J. Sound Vib.*, **65**(2), pp. 275–296.
- [2] Cusumano, J. P., and Kimble, B., 1995, “A Stochastic Interrogation Method for Experimental Measurements of Global Dynamics and Basin Evolution: Application to a Two-Well Oscillator,” *Nonlinear Dyn.*, **8**, pp. 213–235.
- [3] Takens, F., 1981, “Detecting Strange Attractor in Turbulence,” Rand, D. A., and Young, L. S., eds., *Dynamical Systems and Turbulence*, Warwick, Springer Lecture Notes in Mathematics, Springer-Verlag, Berlin, pp. 336–381.
- [4] Sauer, T., Yorke, J. A., and Casdagli, M., 1991, “Embedology,” *J. Stat. Phys.*, **65**(3–4), pp. 579–616.
- [5] Feeny, B. F., Yuan, C. M., and Cusumano, J. P., 2001, “Parametric Identification of an Experimental Magneto-Elastic Oscillator,” Accepted, *J. Sound Vib.*, **247**(5), pp. 785–806.
- [6] Woodson, H. H., and Melcher, J. R., 1968, *Electromechanical Dynamics, pt. 1: Discrete Systems*, Wiley, New York.
- [7] Strauss, E., Golodnitsky, D., and Peled, E., 1999, “Cathode Modification for Improved Performance of Rechargeable Lithium/Composite Polymer Electrolyte-Pyrite Battery,” *Electrochem. Solid-State Lett.*, **2**(3), pp. 115–117.
- [8] Cusumano, J. P., and Chatterjee, A., 2000, “Steps Towards a Qualitative Dynamics of Damage Evolution,” *Int. J. Solids Struct.*, **37**(44), pp. 6397–6417.
- [9] Sanders, J. A., and Verhulst, F., 1985, *Averaging Methods in Nonlinear Dynamical Systems*, Springer-Verlag, New York.